

1 Experimental and theoretical study of bumped characteristics 2 obtained with cylindrical Langmuir probe in magnetized Helium 3 plasma

4 J. Ledig,¹ E. Faudot,¹ J. Moritz,¹ S. Heuraux,¹ N. Lemoine,¹ and M. Usoltceva^{1,2}

5 ¹Université de Lorraine – Institut Jean Lamour, Campus Artem 2 allée André Guinier - BP 50840,
6 54011 NANCY Cedex, France

7 ²Max Planck Institut für Plasmaphysik – Boltzmannstr. 2, 85 748, Garching,
8 Germany

Cylindrical Langmuir probe measurements in a Helium plasma were performed and analysed in the presence of a magnetic field. The plasma is generated in the ALINE device, a cylindrical vessel 1 m long and 30 cm in diameter using a direct coupled RF antenna ($v_{\text{RF}} = 25$ MHz). The density and temperature are of the order of 10^{16} m^{-3} and 1.5 eV, respectively, for 1.2 Pa Helium pressure and 200 W RF power. The axial magnetic field can be set from 0 up to 0.1 T, and the plasma diagnostic is a RF compensated Langmuir probe, which can be tilted with respect to the magnetic field lines. In the presence of a magnetic field, $I(V)$ characteristics look like asymmetrical double probe ones (tanh-shape), which is due to the trapping of charged particles inside a flux tube connected to the probe on one side and to the wall on the other side. At low tilting angle, high magnetic field amplitude, power magnitude and low He pressure, which are the parameters scanned in our study, a bump can appear on the $I(V)$ in the plasma potential range. We then compare different models for deducing plasma parameters from such unusual bumped curves. Finally, using a fluid model, the bump rising on the characteristics can be explained, assuming a density depletion in the flux tube, and emphasizing the role of the perpendicular transport of ions.

9 I. INTRODUCTION

10 Cylindrical Langmuir probes are one of the sim-
11 plest device to investigate plasma properties as they
12 consist of a small metallic wire of length L_p and
13 radius r_p , usually made of tungsten, immersed into
14 the plasma, and submitted to a ramp of voltage. The
15 collected current by the tip vs. the applied voltage
16 yields an $I(V)$ probe characteristics, from which
17 electron density n_e , ion density n_i and temperature
18 T_e can be derived.

19 An $I(V)$ curve can be divided in three parts :
20 the “ion saturation current” part, the “electron sat-
21 uration current” and the exponential part^{1,2}. For
22 strongly negative potentials V applied to the probe
23 (with respect to plasma potential ϕ_p) electrons are
24 repelled and ions accelerated towards the probe, the
25 collected current being the ion saturation current I_i .
26 In the opposite case, $V \gg \phi_p$, only electrons are
27 collected and the measured current at the probe is
28 the electron saturation one I_e . These regions are so
29 called “saturation current” because their mean ve-
30 locities saturate at $\langle v \rangle_{\text{max}}$, deduced from their veloc-
31 ity distribution. Actually even in the saturation part,
32 I keeps on increasing with V , because the sheath
33 surrounding the probe is growing with the applied
34 potential. Thus, the collecting surface for the accel-
35 erated species in the sheath is not the probe surface,
36 but the sheath one. Within the transition region,
37 electrons are repelled according to the Boltzmann
38 factor and $n_e e^{-E/k_B T_e}$, with $E = -e(V - \phi_p)$. An-
39 other important point of the $I(V)$ characteristic is
40 the floating potential, ϕ_{fl} , defined as the probe po-

41 tential for which the same amount of ion and elec-
42 tron are collected, *i.e.* for $I = 0$. Note that the con-
43 vention is to count ion current as negative, and elec-
44 tron current as positive on $I(V)$ plots.

45 Determining the plasma parameters on differ-
46 ent regions listed above requires to use the most
47 appropriate theory for each species. Mott-Smith
48 and Langmuir³ proposed the first model to extract
49 temperature and density from characteristics using
50 the OML theory (Orbital Motion Limited). This
51 theory exploits mainly the ion part of the charac-
52 teristics and was developed with the assumption
53 of large sheaths ($r_p/\lambda_D \ll 1$, for λ_D the Debye
54 length of the repelled species), large ion mean-free-
55 path ($\lambda_{i,\text{mfp}}/L_p \ll 1$) and cold ions ($T_i/T_e \rightarrow 0$).
56 Allen and Bernstein⁴⁻⁶ improved this theory, solv-
57 ing the Poisson equation within the sheath, which
58 was omitted in the OML theory. But it can lead to
59 an overestimation of the ion density by a factor of
60 ten⁷. Laframboise extended the model assuming a
61 velocity distribution function for ions⁸, but this so-
62 phisticated approach does not improve the fits of the
63 experimental ion current with respect to the ABR
64 (Allen Boyd Reynolds) model⁵.

65 The presence of a magnetic field changes
66 strongly the way particles are collected on the
67 probe: the motion of charged particles can be di-
68 vided into a longitudinal ($\parallel \mathbf{B}$) and a perpendic-
69 ular ($\perp \mathbf{B}$) components, with their own tempera-
70 ture. In such magnetized conditions, OML the-
71 ory still holds⁹⁻¹¹ for ions, but the electron part is
72 hardly interpretable¹² due to the distortion of the
73 $I(V)$ curve, leading to an uncertainty on the deter-

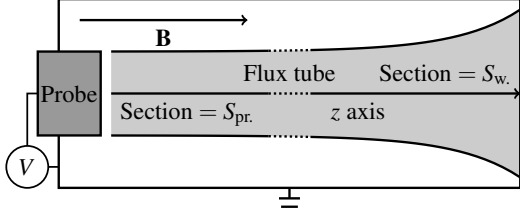


FIG. 1. Illustration of the double probe model : the widening of the flux tube is here to model the fact that at the end of the vessel magnetic field lines drive away each other.

74 mination of ϕ_p and, thus, to a wrong T_e and n_e . Sev-
 75 eral authors^{11,13} emphasized the distortion of the
 76 characteristics in the presence of \mathbf{B} , showing that
 77 I_e is much lower compared to the unmagnetized
 78 case, because electrons are stuck along magnetic
 79 field lines, with a low level of perpendicular trans-
 80 port due to collisions¹⁴ and drain diffusion¹¹ for in-
 81 stance.

82 In several papers it was also reported that, in
 83 some cases, a bump on the characteristics can ex-
 84 ist between the exponential part and the electron
 85 saturation part¹⁵⁻¹⁸. It was assumed that the bump
 86 was caused by a density depletion of the flux tube
 87 during the probing. Dote developed an OML-like
 88 model to explain the presence of the bump^{19,20} and
 89 suggested the plasma potential to be the bump posi-
 90 tion; his model however does not match quite well
 91 with experimental results.

92 The shape of a $I(V)$ characteristic in a mag-
 93 netized plasma can be approached, excluding the
 94 eventual bump, by a double probe model: the per-
 95 fectly confined flux tube (which is $\parallel \mathbf{B}$) is connected
 96 to one hand to the probe, and on the other hand, to
 97 the wall of the reactor as shown in Fig. 1.

98 The collected electron current is mainly paral-
 99 lel to \mathbf{B} while the ion current is perpendicular to
 100 \mathbf{B} so that the lateral surface of the flux tube plays
 101 the role of the wall in a classic unmagnetized dis-
 102 charge. The magnetized double probe model can
 103 then be seen as a classic asymmetric double probe
 104 model without magnetic field²¹. The effect of these
 105 ionic perpendicular currents both in DC^{22,23} and in
 106 RF^{24,25} have already been studied for planar probes.
 107 It was shown that the shape of the $I(V)$ curve was
 108 changed by feeding or pumping the flux tube and
 109 that I-Vs are really sensitive to the r_p/r_L ratio.

110 Here simple asymmetric model is 1D in the z di-
 111 rection (see sketch fig.1), the probe is located at
 112 $z_{pr} = 0$ and the wall at $z_w = L_t$, the length of the
 113 flux tube is then L_t and $\mathbf{B} = B \mathbf{e}_z$. The probe po-
 114 tential is at V , the space potential is ϕ_t and the wall
 115 is grounded. The section of the tube on the wall
 116 side is S_w , and the section at the probe is S_{pr} with

117 $S_{pr} \leq S_w$. We assume constant density in the tube,
 118 n_t , and no loss in the perpendicular direction. Thus,
 119 the stationary ($\partial_t n = 0$) continuity equation writes :

$$\nabla \cdot \mathbf{J}_{\text{Tot.}} = 0 \quad \text{where } \mathbf{J}_{\text{Tot.}} = \mathbf{J}_e + \mathbf{J}_i \quad (1)$$

120 For homogeneous current density across both ends,
 121 using Gauss's theorem by integrating eq.(1) over
 122 the whole flux tube gives :

$$J_{\text{Tot.}}(z=0) \times S_{pr} + J_{\text{Tot.}}(z=L_t) \times S_w = 0 \quad (2)$$

Ion current density is the Bohm flux,

$$J_i = 0.61 \times en_t c_s \quad \text{where } c_s = \sqrt{\frac{k_B T_e}{m_i}},$$

and for electron it is given the Boltzmann equilib-
 rium with the local potential,

$$J_e = -\frac{1}{4} en_t \langle v_e \rangle \times \exp \left[e \frac{\phi(z) - \phi_t}{k_B T_e} \right]$$

$$\text{where } \langle v_e \rangle = \sqrt{\frac{8k_B T_e}{\pi m_e}}.$$

123 Introducing the electron saturation current as
 124 $J_{e,\text{sat.}} = en_t \langle v_e \rangle / 4$ and the floating potential, $\phi_{fl.} =$
 125 $k_B T_e \ln(J_i / J_{e,\text{sat.}}) / e$, eq.(2) becomes :

$$\phi_t = \frac{k_B T_e}{e} \ln \left[\frac{\Sigma + \exp(eV/k_B T_e)}{\Sigma + 1} \right] - \phi_{fl.}, \quad (3)$$

126 where $\Sigma = S_w / S_{pr}$. Finally, the collected current on
 127 the probe is

$$J_{pr}(V) = J_{e,\text{sat.}} \exp \left[e \frac{V - \phi_t(V)}{k_B T_e} \right] - J_i. \quad (4)$$

128 Thus, using eq.(3) in eq.(4) one will get :

$$J_{pr}(V) = J_i \times \frac{\exp(eV/k_B T_e) - 1}{1 + \frac{1}{\Sigma} \exp(eV/k_B T_e)} \quad (5)$$

129 The asymmetric double probe $I(V)$ characteristics
 130 from eq.(5) is plotted in fig.2.

131 In this paper, we investigate the general be-
 132 haviour of "bumped characteristics" with respect
 133 to several parameters, such as the amplitude of the
 134 magnetic field, the gas pressure or the RF power
 135 input. We also propose a new explanation of
 136 the bump, with the aim of a better understanding
 137 of Langmuir probe measurements in magnetized
 138 plasma. In the first part sect.II, the experimental
 139 set-up and the plasma parameters (mean free paths,
 140 Larmor radii, etc.) are detailed. Then the main ex-
 141 perimental results are shown in section III, where
 142 the behaviour of the bumps was studied with respect
 143 to the amplitude of the magnetic field in sect.III A,
 144 the angle ϑ between the probe and \mathbf{B} in sect.III B,
 145 the RF-power input in sect.III C, the probe position

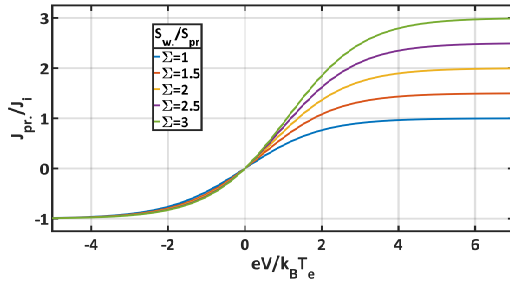


FIG. 2. Theoretical and normalized double probe characteristics for several values of Σ . For $\Sigma \neq 1$ the characteristics are called “asymmetric”, and for $\Sigma \rightarrow \infty$ they are very similar to classical Langmuir characteristics (S_w is the surface of the whole vessel in that case).

146 with respect to the RF-antenna in sect.III D and fi-
 147 nally the He pressure in sect.III E. In the follow-
 148 ing, sect.III, a method is proposed to determine the
 149 plasma temperature and density with conventional
 150 methods (when no magnetic field is present). Fi-
 151 nally, the origin of the bump characteristics is ex-
 152 plained thanks to a fluid model in the last section.

153 II. EXPERIMENTAL SETUP

154 Experiments were performed in the ALINE^{26,27}
 155 (A LINEar plasma device) reactor (see figure 3 and
 156 4). The cylindrical chamber is 1 m long and 30 cm
 157 diameter. The typical discharges presented here are
 158 generated by a RF-antenna at $\nu_{RF} = 25$ MHz (but
 159 the amplifier frequency can be tuned from 10kHz
 160 to 250 MHz), and the RF-power is in the range 20
 161 - 200 W (though 0 to 600 W is achievable). The
 162 amplifier is directly connected to the antenna (direct
 163 coupling, so the average potential on the antenna is
 164 0 V). The cathode is at the center of the vessel has
 165 a radius of 4 cm and is 1 cm thick.

166 Six circular coils generate an axial magnetic field
 167 from 0 to about 100 mT (the current in the coils is
 168 in the range 0–200 A). Helium gas was used for
 169 all discharges with a pressure in the range between
 170 1.2 and 40 Pa for this study, which allows the study
 171 from collisionless to collisional regimes.

172 The cylindrical Langmuir probe Tungsten tip
 173 used in measurements has a length L_p of 1 cm and a
 174 radius r_p of 75 microns. To enable measurements in
 175 a RF plasma, the probe is RF-compensated^{7,28}. For
 176 each $I(V)$ characteristics, a voltage ramp from -70
 177 to 70 V is swept 20 times at a frequency of the order
 178 of 65 kHz. Hence, the measurement frequency
 179 is much slower than RF-oscillations and all plasma
 180 frequencies (ω_e and ω_p), and thus, can be seen as
 181 “stationary” with respect to the plasma dynamics.

182 The position of the probe tip is given with re-
 183 spect to the middle of the antenna ($y = 0$ and $z = 0$).

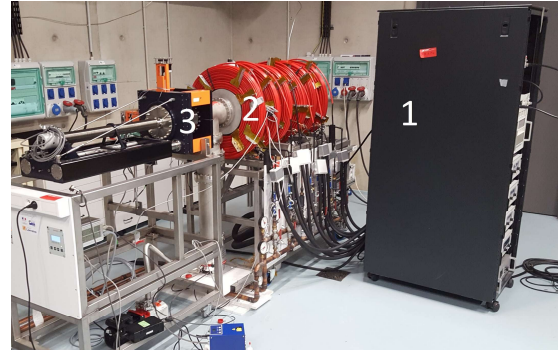


FIG. 3. Photograph of the ALINE plasma device. The cylindrical vessel (2) is 1m long and 30 cm diameter. Six coils (in red) are placed equidistantly along the axis, around the chamber to generate a quasi-homogeneous and uniaxial magnetic field along the axis of the cylinder. The power supplies for the coils and the RF antenna are placed in the rack (1). The antenna is in the middle of the vessel. The arm (3) holding the Hidden Langmuir probe along the vessel’s axis was developed by Cryoscan and is able to perform 3D translations (along the axis, up/down and left/right). Note that the arm is always parallel to the axis of the cylinder.

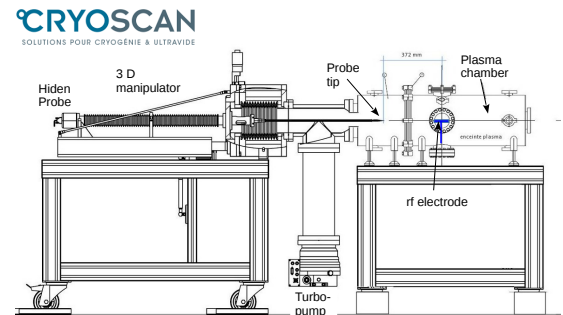


FIG. 4. Schematic representation of the plasma device designed by Cryoscan. The gas inlet is on the top-right end of the device (on the opposite of the pump).

184 All measurements were performed at $z = -60$ mm
 185 along the axis of the cylindrical chamber and $y = 40$
 186 mm above the antenna. The arm holding the probe
 187 is parallel to the axis of the cylindrical vessel, and
 188 only the tip is tilted ϑ with respect to the magnetic
 189 field lines (see fig.5). $\vartheta \in [0, 6, 12, 18, 40, 94]^\circ$
 190 angles were used for the study.

191 Moreover, the arm (see (3) in figure 3) is able
 192 to move the probe tip inside a volume (see the red
 193 dashed box in figure 6) to get three-dimensional
 194 measurements of plasma parameters. Solving Biot-
 195 Savart law in the whole vessel gives the magnetic
 196 field topology. Figure 6 shows the result of the
 197 computation. Let $\langle B \rangle_{\text{meas.}}$ be the averaged modulus
 198 inside the workable volume : in this paper we as-
 199 sume uniaxial (along z , the axis of the reactor) and

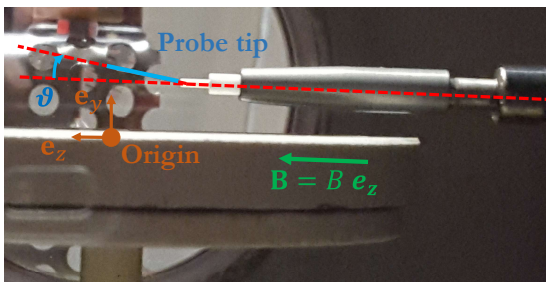


FIG. 5. Tilted cylindrical Langmuir probe with an angle $\vartheta = 12^\circ$ with respect to \mathbf{B} (which is assumed homogeneous and constant in the whole probed volume, $\mathbf{B} = B\mathbf{e}_z$). The position of the probe is $z = 0$ and $y = 5$ mm on this photograph. The value of the angle with respect to the antenna was measured thanks to the open source GeoGebra software.

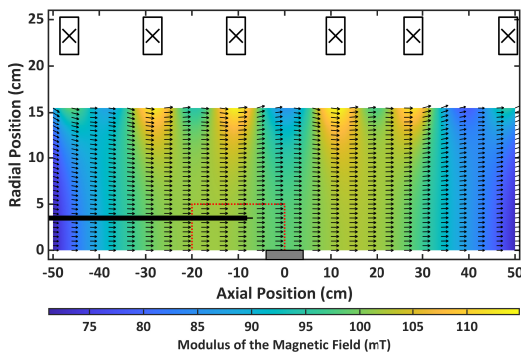


FIG. 6. Magnetic topology in the ALINE plasma device. The gray rectangle at the bottom represents the RF cathode, the long black rectangle and the narrow line at its end at $r = 4$ cm represents the probe and its arm at probing position $(x, y, z) = (0, 40, -60)$ mm. The red dashed box delimits the workable volume. White arrows represent the local magnetic field vectors.

constant magnetic field (the deviation from the averaged value being less than 3% in the probed volume). In the following $B = \|\mathbf{B}\| = \langle B \rangle_{\text{meas.}}$, and $\mathbf{B} = B\mathbf{e}_z$.

In low pressure conditions, $p = 1.2$ Pa, the plasma can be considered as collisionless. Indeed after the values listed in table I, electron mean free path is greater than the probe dimensions⁶, *i.e.* $\lambda_{e,\text{mfp}} \gg r_p$ and L_p . Ions can be considered as unmagnetized for the probe since $\rho_{ci} \gg r_p$. Note that an electron needs a parallel velocity over $L_p \omega_{ce}/2\pi \approx 2.8 \times 10^7$ m/s to overfly the probe without completing a cyclotron period: at this velocity the $f_e(\mathbf{v}) \sim 0$, which means that almost all electrons complete an entire turn over the length of the probe. The electron collection can thus be seen as the intersection of the “cyclotron disk” ($\pi\rho_{ce}^2$) with the probe for parallel inclination in collisionless regimes.

TABLE I. Plasma parameters for $\|\mathbf{B}\| = 100$ mT and $p = 1.2$ Pa. Note that probe dimensions are $r_p = 75$ μm and $L_p = 1$ cm, ρ_c is the Larmor radius, λ_{mfp} is the mean-free-path for charged particle/neutral collisions, ν_c the cyclotron frequency ($\omega_c/2\pi$), ν_p the plasma frequency and ν_{col}^N the charged particle/neutral collision frequency^{29,30}.

Quantity	Ions He^+	Electrons e^-
T (eV)	0.026	2 – 4
n (m^{-3})	$5 - 50 \times 10^{15}$	$5 - 50 \times 10^{15}$
ρ_c (μm)	400	37 – 83
λ_{mfp} (cm)	1.50	2 – 4.5
ν_c (Hz)	380×10^3	3×10^9
ν_p (Hz)	$7 - 23 \times 10^6$	$635 - 2000 \times 10^6$
ν_{col}^N (Hz)	88×10^3	$38 - 85 \times 10^6$

III. EXPERIMENTAL STUDY

Scans over B , ϑ , RF-power, y -position and pressure were performed and main results are presented here. If not specified the probe tip position is set by default at $y = 40$ mm and $z = -60$ mm, and the pressure at 1.2 Pa.

A. Influence of the magnetic field

$I(V)$ Characteristics for all inclinations of the probe tip have been plotted for several values of $\|\mathbf{B}\|$ and for a 200 W-RF power input in fig.7. Without magnetic field (fig.7-(a)), the “classical” $I(V)$ is recovered, because the plasma is an isotropic medium and the orientation of the probe unimportant. The slight differences between all six curves come from small variations on the plasma conditions, due to the fact that the change of inclination requested to open the chamber between each measurement (uncertainties within 5% due to the gas pressure gauge, thus the RF coupled power which is sensitive to the pressure may not be exactly the same).

The shape of the $I(V)$ changes drastically in the presence of a magnetic field as depicted in fig.7-(b) to (d). The slope of the exponential part and the electron saturation current one as well as the ratio I_e/I_i are strongly affected by the addition of a magnetic field¹¹. Note that the increase of I_e with the magnetic field is due to a better coupling of the RF power and to better confinements. More generally, it can be seen that the overall shape of the characteristics are qualitatively close to the double probe/tanh-shape ones modelled by eq.(5). For small angles ($\vartheta \leq 12^\circ$), the characteristics even display a bump between the exponential and the saturation parts. The bump’s overshoot amplitude and the change in the slope between the exponential part

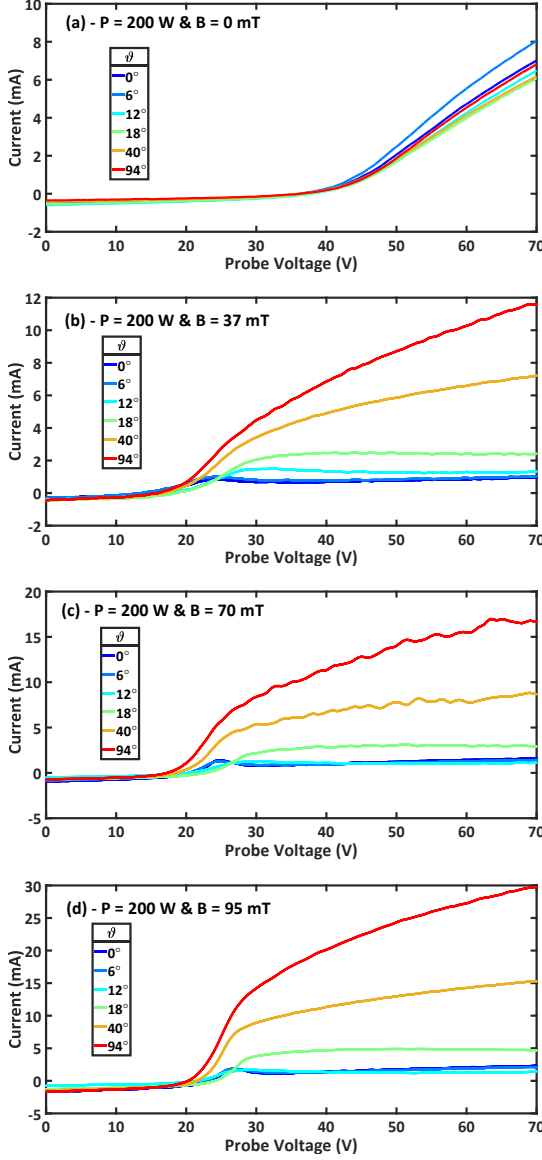


FIG. 7. Evolution of the $I(V)$ characteristics at 200 W-RF power, at position $y = 40/z = -60$ mm with increasing $\|\mathbf{B}\|$ from 0 (a) to 95 mT (d) for all six ϑ inclinations, 1.2 Pa He. Potential range of the measurements were -70 to $+70$ V, but the purpose of the study is not the ion part so only the range $[0, 70]$ V is displayed here. Note that the current range changes for each graphs.

256 and the electron saturation regime is emphasized
257 and steeper with larger $\|\mathbf{B}\|$.

258 B. Influence of probe inclination

259 For a probe inclination of 18° , the measured $I(V)$
260 characteristic looks like the “tanh-shape” as ex-
261 plained previously. For higher inclination angle, the
262 electron current does not saturate (due to sheath ex-

263 pansion) and for lower inclination angle, there is a
264 bump. The only difference between all these dif-
265 ferent cases is the width of the flux tube that scales
266 as $\sim L_p \sin \vartheta$. The probe area facing magnetic field
267 lines (see fig.5) is written as follows :

$$S_{\text{face}} = \pi r_p^2 \cos \vartheta + \pi L_p r_p \sin \vartheta \quad (6)$$

268 which can be scaled as $S_{\text{face}} \sim \sin \vartheta$ because $L_p \gg$
269 r_p .

270 For $\vartheta = 0^\circ$ at 100 mT, $r_p \approx 2\rho_{ce}$, therefore, the
271 probe surface facing the magnetic flux tube is compar-
272 able to the “cyclotron area” ($S_{ce} = \pi\rho_{ce}^2$) : in
273 this case of grazing incidence, a bump arises on
274 the measured characteristics. By increasing the an-
275 gle, the facing surface increases (whereas the cyclo-
276 tron area remains constant) and the amplitude of
277 the bump decreases, and even disappears for larger
278 angles. One can suggest that the flux tube nar-
279 rowness comparable to the cyclotron area could ex-
280 plain the bump. However, it remains even if $S_{\text{face}} \gg$
281 S_{ce} (when $\vartheta > 5^\circ$), therefore another mechanism
282 should be invoked in order to explain the presence
283 of the bump.

284 We performed a series of experiments with a
285 power input in the range 20 - 200 W in order to
286 quantify the evolution of the characteristics with re-
287 spect to ϑ . Fig.8 shows the evolution of the current
288 at 70 V, $I(V = V_{\text{max}} = 70 \text{ V})$ or the “end-current”,
289 against $\sin \vartheta$. This end value is used, because the
290 plasma potential is actually unknown, so the compar-
291 ison of the current at plasma potential is not possi-
292 ble for now.

293 Without magnetic field (fig.8-(a)), the *end-*
294 *current* is constant for any inclination as explained
295 previously. Moreover by increasing the RF-power,
296 the overall collected end-current also increases, be-
297 cause the power also increases the plasma density
298 ($I \propto n_e$) as expected.

299 In the presence of a magnetic field of 95 mT
300 (fig.8-(b)) two regimes are evidenced : the region
301 where there is a bump ($\vartheta \leq 12^\circ \Leftrightarrow \sin \vartheta \leq 0.21$)
302 and the region with an asymmetric double probe
303 behaviour (above 12°). In the former region, the
304 end current is proportional to $\sin \vartheta$, as the width
305 of the magnetic flux tube : the sine dependence of
306 the current collection is verified. But in the “bump
307 region”, the collected end-current remains approxi-
308 mately constant with ϑ for any RF-power. Since
309 the collected current is proportional to the product
310 of the density with the collecting surface, $n_e S_{\text{coll}}$,
311 (assuming $\langle v_e \rangle \sim \langle v_{e,\parallel} \rangle \approx \text{Cte.}$), the increase of the
312 angle also increases S_{coll} , so to keep constant col-
313 lected current, the electron density in the flux tube
314 should decrease. This is in a good agreement with
315 figure 9-(b): in the presence of a magnetic field, and
316 if there is a bump on the characteristic, the density
317 is lower than in the absence of a bump (going from

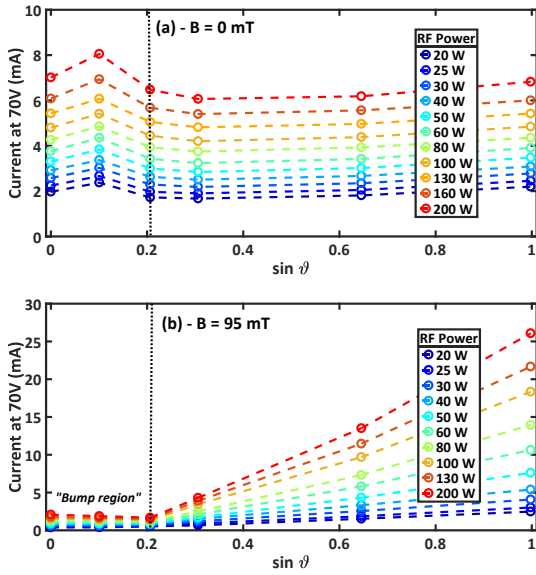


FIG. 8. Evolution of the collected current at 70 V with the sine of the inclination angle ϑ without magnetic field (a), and with magnetic field (b) of amplitude 95 mT, 1.2 Pa He. The left region is the “bump region”, where a bump is measured ($\vartheta \leq 12^\circ \Leftrightarrow \sin \vartheta \leq 0.21$). The line is a guide for the eye.

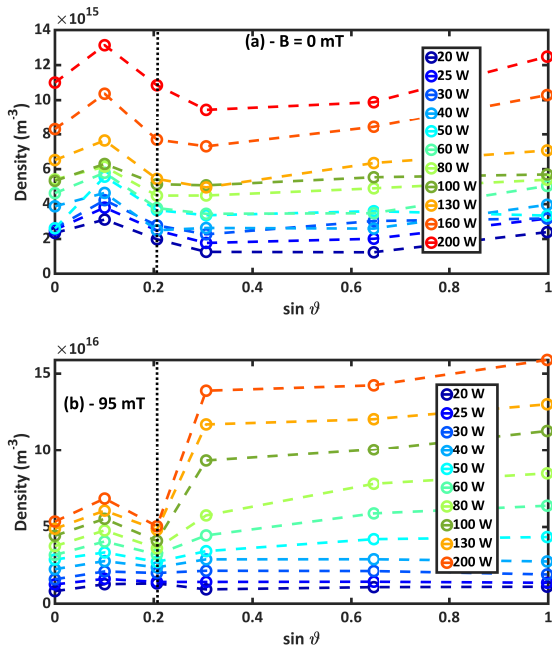


FIG. 9. Evolution of the density measured with the method described in the next section, in same conditions as in figure 8 with magnetic field (a) and without magnetic field (b) of 95 mT. As expected, the density is kept approximatively constant in the absence of magnetic field, but we notice a sharp change in the density between the “bump-” and the “no-bump-region” in the presence of magnetic field at higher power. The line is a guide for the eye.

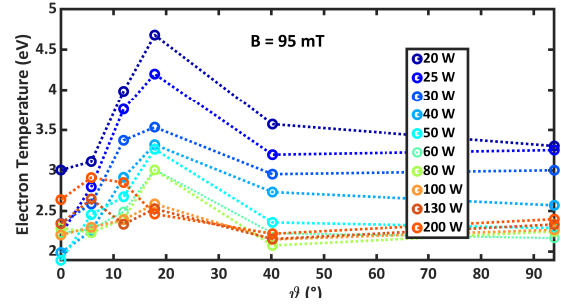


FIG. 10. Evolution of the computed electron temperature (see next section for the used algorithm) with respect to the inclination of the probe at 95 mT magnetic field amplitude. The line is a guide for the eye.

318 $n_e \approx 5 \times 10^{15} \text{ m}^{-3}$ with a bump to $n_e \approx 15 \times 10^{15}$
 319 m^{-3} without a bump at 200 W RF power). This
 320 density difference is enhanced for higher power.
 321 However, for lower power the density remains app-
 322 proximatively constant at all inclinations.

323 However, the evolution of the electron tempera-
 324 ture with respect to the inclination angle (figure
 325 10) is impossible to explain straightforwardly. In-
 326 deed the electron flow collected by the probe is the
 327 combination of two populations: the parallel and
 328 the perpendicular to B flow, having each its own
 329 temperature (i.e. $T_{e\parallel}$ and $T_{e\perp}$ resp.). Our method
 330 gives a kind of average of both. Unfortunately, the
 331 electron energy distribution function, which could
 332 help us to understand the plot, is too noisy to be ex-
 333 ploited (even after some filtering such as Stavitzky
 334 Golay, or Fourier analysis). The explanation of this
 335 plot is still an opened question for further studies.

336 Nevertheless, constant end-current in bump -
 337 region can also mean there is a surrounding electron
 338 sheath assuming the probe potential is higher than
 339 the plasma potential, and then the effective collect-
 340 ing radius is higher than the probe radius.

341 C. Influence of the RF-power

342 As shown in the last subsection, increasing RF-
 343 power also increases the overall density. To track
 344 the bump evolution with RF-power regardless to
 345 the density change, it is convenient to normalize
 346 the $I(V)$ to the end-current value $I(V)/I(70 \text{ V})$. In
 347 fig.11 are depicted the normalized probe character-
 348 istics at $\|\mathbf{B}\| = 95 \text{ mT}$ for all inclinations and for
 349 several input RF-power, fig.11-(a) to (c).

350 Although the end current is proportional to the
 351 collecting surface (which is $\propto \sin \vartheta$), the normal-
 352 ization removes this dependence and all angles can
 353 be compared. The electron saturation part, directly
 354 connected to the sheath extension, is then the same
 355 for every angles, as shown in fig.11. In fig.11-(a),

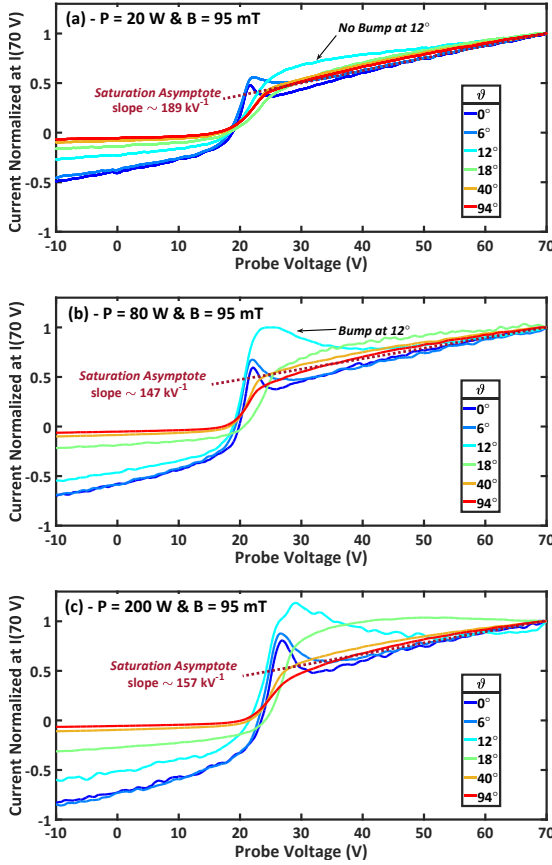


FIG. 11. Normalized $I(V)/I(V_{\max})$ characteristics at 95 mT, for every inclination angles, 1.2 Pa He. RF-power is fixed at (a) 20 W, (b) 80 W and (c) 200 W. On each graph is also plotted (on dashed lines) the mean saturation linear curve with its slope.

356 for 20 W there is no bump at 12° , contrary to fig.11-
 357 (b) for 80 W. The current at the bump position is
 358 also larger than the end-current in fig.11-(c). More-
 359 over, the increase of the power increases the ampli-
 360 tude of the bump and its width.

361 One can suppose the existence of perpendicular
 362 (to \mathbf{B}) RF currents, pumping the flux tube con-
 363 nected to the probe: this idea is used to derive
 364 a fluid model in section IV to recover the bump
 365 analytically. In addition, as depicted in fig.8-(b),
 366 increasing the power does not increase the end-
 367 current in the “bump region”, corroborating the for-
 368 mer assumption. These RF currents, when averaged
 369 over one RF period, exhibit a net DC perpendicular
 370 contribution³¹, acting as perpendicular DC cur-
 371 rents, which have already been investigated in pre-
 372 vious models^{22,23} to explain the depletion and satu-
 373 ration currents of biased flux tubes.

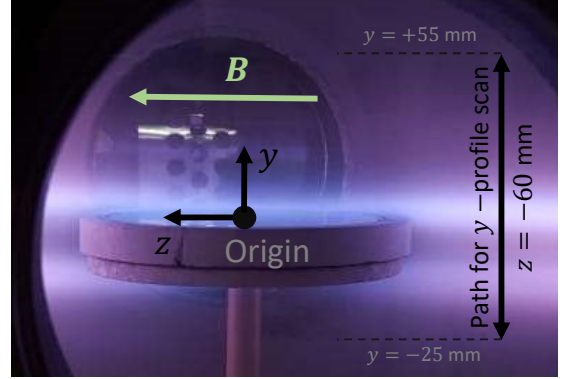


FIG. 12. Photograph from 1.2 Pa He pressure plasma around the RF antenna operating at 100 W with $\|\mathbf{B}\| = 80$ mT magnetic field. The magnetic confinement generates this double player plasma aspect around the probe. Far enough from the antenna the density is homogeneous.

374 D. Influence of the probe position

375 The position of the probe is also an important
 376 parameter. It is initially placed relatively far from
 377 the antenna to have a homogeneous plasma around
 378 the probe. Indeed, near the antenna, the $\mathbf{E} \times \mathbf{B}$
 379 effect is larger and the plasma denser. That is why,
 380 there is a thin plasma layer above, and below the
 381 antenna (see photograph in fig.12). Moreover, at
 382 this RF-pulsation ions do not react to the quick po-
 383 tential change near the antenna, whereas electrons
 384 do³² ($\omega_{pe} > \omega_{RF} > \omega_{pi}$).

385 To make sure that the inclination of the probe
 386 does not scan different slices of plasma (i.e. that
 387 the plasma is homogeneous in a range of $\pm L_p \sin \vartheta$
 388 around the probing position in the y direction), mea-
 389 surements along the y axis were performed at fixed
 390 $z = -60$ mm position and for $\vartheta = 0^\circ$. Power was
 391 fixed at 100 W-RF, $\|\mathbf{B}\| = 80$ mT in 1.2 Pa He
 392 plasma. All characteristics in Fig.13 depicted a
 393 bump, where the plotted parameters are the float-
 394 ing potential ϕ_{fl} , the bump potential V_{bump} and the
 395 bump current I_{bump} . Dote suggested the bump po-
 396 tential to be near the plasma one^{15,19,20}. According
 397 to Dote’s assumption and using the combined po-
 398 tential drops in the sheath and the collisionless pre-
 399 sheath¹, one can write the potential drop between
 400 the plasma and the floating probe potential for cold
 401 ions ($T_i/T_e \rightarrow 0$) as:

$$\phi_p - \phi_{fl} = \frac{T_e}{2e} \ln \left[\frac{m_i}{2\pi m_e} \right] + \frac{T_e}{2e} = 4.03 \times T_e, \quad (7)$$

402 with T_e in eV. For all previous measurements at
 403 ($z = -60$ mm, $y = 40$ mm), using the approxima-
 404 tion $\phi_p \approx V_{\text{bump}}$ gives $T_e \approx 1.30$ eV (which is a typ-
 405 ical value in ALINE magnetized, plasma^{26,27}).

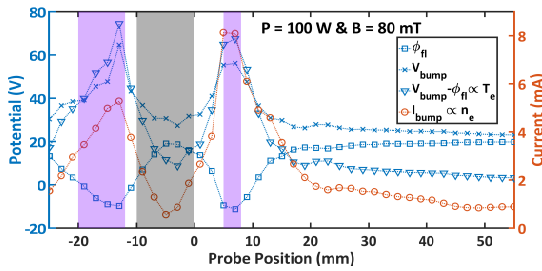


FIG. 13. Evolution of measured parameters (floating potential ϕ_f , bump potential V_{bump} and bump current I_{bump}) along the y axis at $z = -60$ mm, 100 W-RF, 80 mT and 1.2 Pa (see double arrow \leftrightarrow in fig.12). The gray region represents the region where the probe faces the antenna (antenna extension is $z \in [-40, 40]$ mm and $y \in [-10, 0]$ mm), the purple regions represent the denser plasma region (see photograph in fig.12). For comparison $T_e \propto V_{\text{bump}} - \phi_f$ is also plotted.

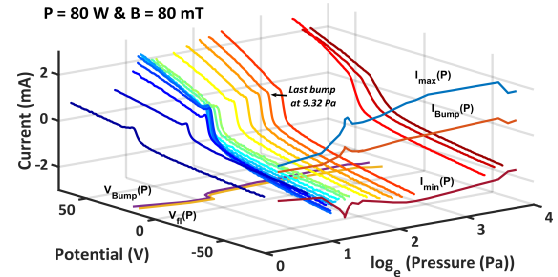


FIG. 14. Tridimensional representation of the $I(V)$ characteristics in all considered He pressures from 1.2 to 40 Pa for 80 W-RF power and $||\mathbf{B}|| = 80$ mT. In the $V = 80$ V plane are plotted the end currents at ± 70 V and the bump current. In the $I = -3$ mA plane are plotted the floating and the bump potentials. Last bump is measured at 9.32 Pa. If no bump is measured, I_{bump} corresponds to the point where $dI/dV = \max(dI/dV)$, i.e. the current at “classical” plasma potential.

407 The tilting of the probe does not scan “different
408 slices” of plasma and different inclination angles
409 can be compared as shown in fig.13: 1 cm around
410 the $y = 40$ mm position, all cited parameters are
411 almost constant. Therefore, the homogeneity hypo-
412 thesis (almost constant T_e and n_e in the probing
413 area) can be applied in the experimental conditions.
414 Finally, this last figure also highlights the fact that
415 current and temperature (as defined in eq. 7) in-
416 creases by a factor of ~ 7 in the bright regions (see
417 photograph depicted in fig.12), near the antenna.

418 E. Influence of the pressure

419 For a magnetic field of 80 mT, and an input
420 power of 80 W-RF, measurements were performed
421 with a probe parallel to the field line ($\vartheta = 0^\circ$) in a
422 He pressure range from 1.2 to 40 Pa. All character-
423 istics are plotted Fig. 14.

424 When pressure increases, the bump gets narrower
425 and its amplitude diminishes. Above 9.32 Pa, the
426 bumps disappear and the $I(V)$ characteristic turns
427 into an asymmetric double probe one.

428 That’s why one can separate the pressure range
429 in 2 regimes :

430 The low collisional regime from 1 Pa to 10
431 Pa. At these pressures the electron–neutral col-
432 lision frequency ν_{col}^{eN} is lower than the electron
433 plasma frequency ν_{pe} , and lower than the electron
434 cyclotron frequency ν_{ce} (see table I) and of the same
435 order than the RF frequency. For example at 1 Pa
436 $\nu_{\text{col}}^{eN} \approx 17$ MHz²⁹. In the same way the ion-neutral
437 collision frequency ν_{col}^{iN} is much lower than the ion
438 plasma frequency ν_{pi} , and lower than the ion cy-
439 clotron frequency ν_{ci} up to 4 Pa so that ions are
440 considered as magnetized in the first half of the low
441 collisional pressure range. In this range the classi-

442 cal perpendicular diffusion falls down and perpen-
443 dicular currents are able to deplete strongly the flux
444 tube while the typical scale length of these current
445 is higher than the radius of the probe, which is the
446 case here because $\rho_{ci} \gg r_p$. In a quiet plasma, as
447 we have in ALINE, such a behaviour can be seen,
448 while in Tokamak edge plasma anomalous transport
449 can still prevent the biased flux tubes to deplete.

450 In the collisional regime ($P > 10$ Pa), ν_{col}^{eN} re-
451 mains lower than ν_{ce} and ν_{pe} , but much higher than
452 the RF frequency. RF electron current are then low-
453 ered by collisions. And ions are no more magne-
454 tized because $\nu_{\text{col}}^{iN} > \nu_{ci}$, which favours their per-
455 pendicular diffusion while ion perpendicular cur-
456 rent are lowered in the same time, filling the lack
457 of density caused by the probe collection and can-
458 celling the bump on the characteristics. For the
459 highest pressures, the flux tube for ions disappears
460 and the $I(V)$ looks like an unmagnetized one¹⁴.

461 In the intermediate case of partially magnetized
462 ions, the $I(V)$ looks like a double symmetric probe
463 characteristics. The electron saturation current col-
464 lected by the probe depends also on the competition
465 between perpendicular DC and RF currents and the
466 cross diffusion of ions due to collisions.

467 Another remarkable result depicted in fig.14 is
468 that, when the pressure is increased by a factor of
469 40, the maximal current at probe position only in-
470 creases by a factor 2. This behaviour denotes a good
471 confinement of the plasma around the antenna by
472 the magnetic field. Indeed, increasing the pressure
473 brightens the plasma shown in fig.12; however out-
474 side this region the plasma remains more or less the
475 same. The only thing that changes is the collision
476 rate with neutrals at higher density.

477 IV. THEORETICAL APPROACHS

478 In the first part of this section, we provide a quan-
 479 titative comparison of three different methods used
 480 to extract both n_e and T_e from bumped character-
 481 istics. In a second part, we show by using a fluid
 482 model that, the bump in the $I(V)$ curves in a pres-
 483 ence of a magnetic field, can be explained by mean
 484 of density depletion within the tube flux connected
 485 to the probe and to the opposite wall of the reactor.

486 A. Density and temperature data processing

487 Extracting electron density and temperature from
 488 $I(V)$ characteristics is far from simple. But if
 489 the measurements are done in the presence of
 490 a magnetic field, the exploitation are even more
 491 difficult. The challenge lies on the presence of
 492 the bump, whose existence, shape, location and
 493 amplitude depend on several plasma parameters
 494 ($|\mathbf{B}|$, ϑ , $P_{\text{wr.}}$, y , p) (see sections III A to III E).

495 The first problem with bumped characteristics is
 496 the uncertainty on the position of the plasma po-
 497 tential. It is usually found by assuming that, at the
 498 plasma potential $V = \phi_p$, $dI/dV|_{\phi_p} = \max(dI/dV)$,
 499 which is equivalent to $d^2I/dV^2|_{\phi_p} = 0^{2,3}$ (this is
 500 called the ‘‘classical method’’ in the following). An-
 501 other method based on the intersection of the linear
 502 fits of the exponential part and the electron satu-
 503 ration one has also been suggested and used in a pre-
 504 vious study¹⁷. It was finally suggested that, in the
 505 context of bumped characteristics, the bump po-
 506 tential is at the plasma potential^{15,19}. Thus, three meth-
 507 ods are available, in order to determine the plasma
 508 potential and we propose to compare them, for dif-
 509 ferent inclinations, in a single 100 W-RF plasma,
 510 with $|\mathbf{B}| = 80$ mT and $p = 1.2$ Pa, whose charac-
 511 teristics are depicted in fig.15-(a).

512 We assume that the best method is the one which
 513 would exhibit the lowest deviation of the plasma pa-
 514 rameters with respect to ϑ . We suppose indeed that
 515 the probed plasma slice is the same for all inclina-
 516 tions.

517 In the context of the ‘‘intersection method’’
 518 we linearised the exponential growth as $I(V) \approx$
 519 $a_{\text{exp.}}V + b_{\text{exp.}}$, and fitted the electron saturation cur-
 520 rent with the formula:

$$I_e(V) \approx a_{\text{sat.}}V + b_{\text{sat.}} + c_{\text{sat.}}\sqrt{V}. \quad (8)$$

521 with the \sqrt{V} term similar to one of the OML ap-
 522 proach, which gives a relatively good fit with exper-
 523 imental curves. This equation is only able to fit
 524 the saturation part, *i.e.* the end of the $I(V)$ — far
 525 from the bump potential range. Only the last 20
 526 volts of each $I(V)$ were used for the fitting, see fig.
 527 15-(a).

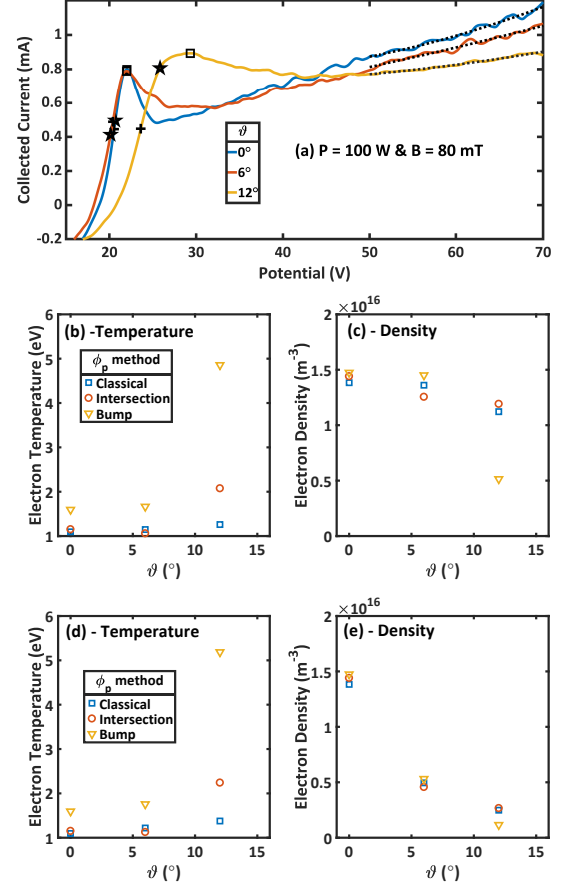


FIG. 15. Results of the electron temperature and density calculation on bumped characteristics with the described iterative model : (a) $I(V)$ of plasma at 100 W-RF, 80 mT and 1.2 Pa for different probe inclinations and all methods are represented for the position of ϕ_p (+ classical, \star intersection, \square bump). The dashed line is the fit of the electron saturation current with respect to equation (8) – (b) and (c) T_e and n_e against inclination angle with collecting surface correction – (d) and (e) T_e and n_e against inclination angle without collecting surface correction, $S_{\text{coll.}} = S_{\text{probe}}$ (T_e remains the same though).

528 We used an iterative method, in order to deter-
 529 mine both n_e and T_e with the plasma potential ϕ_p ,
 530 the current at plasma potential I_p , floating poten-
 531 tial $\phi_{\text{fl.}}$, magnetic field and probe inclination as
 532 input parameters. First, a raw approximation of
 533 electron temperature is done, supposing $I \sim I_e \propto$
 534 $\exp(eV/k_B T_e)$ for $V \leq \phi_p$ in the exponential part.
 535 Applying a linear fit on $\ln I(V)$ one will find a first
 536 value of T_e . From now one starts the iterative loops:
 537 this electron temperature value allows a computa-
 538 tion of a gross value of n_e since, at plasma potential,
 539 $I_p = en_e(v)S_e/4$. The value of S_e is not the probe
 540 surface, even at plasma potential (where there is no
 541 sheath), because of the cyclotron motion. That is
 542 why it is assumed that the collecting surface is the

543 probe surface facing \mathbf{B} plus a layer thick of $N_{\text{elr.}}\rho_{ce}$
 544 (i.e. some Larmor radii – $N_{\text{elr.}}$ being the number of
 545 electron Larmor radii connected to the probe) :

$$S_e = \pi \cos \vartheta \times (r_p + N_{\text{elr.}}\rho_{ce})^2 + \pi L_p \sin \vartheta \times (r_p + N_{\text{elr.}}\rho_{ce}) \quad (9)$$

546 by replacing $r_p \rightarrow r_p + N_{\text{elr.}}\rho_{ce}$ in eq.(6). It is as-
 547 sumed that this equation takes into account the per-
 548 pendicular motion of electrons along the magnetic
 549 field lines connected to the probe.

550 With T_e and n_e , it is possible to compute the elec-
 551 tron Debye length λ_{De} and the ion sheath thickness
 552 using the Child-Langmuir law (since $\rho_{ci} \gg r_p \sim \rho_{ce}$
 553 and that Zhu's corrections³³ for cylindrical geome-
 554 try only bring minor changes in opposition to its
 555 complexity), knowing,

$$\ell_{\text{CL}} = \frac{\sqrt{2}}{3} \lambda_{\text{De}} \left(2e \frac{|\phi_p - V|}{k_B T_e} \right)^{3/4} \quad (10)$$

556 for $V \leq \phi_p$. Since ions are supposed unmagnetized,
 557 the collecting area for ions is

$$S_i = \pi(r_p + \ell_{\text{CL}})^2 + 2\pi L_p(r_p + \ell_{\text{CL}}). \quad (11)$$

558 It is then possible to compute the ion current
 559 for $V \leq \phi_p$, using the Bohm flux formula, $I_i =$
 560 $0.61 \times en_e c_s S_i$. So, the updated electron current
 561 $I_e = I(V) - I_i$ can be calculated. Taking again the
 562 log-scale of this new electron current gives a new
 563 more accurate value of T_e . The loop starts over
 564 again, and ends if temperature values converge (i.e.
 565 $|T_e^{\text{new}} - T_e^{\text{old}}| \leq \varepsilon$, ε being given by the user).

566 Equations giving S_e and S_i (eqs. (9) and (11)
 567 resp.) take into account the sheath extension for
 568 magnetized electrons and unmagnetized ions. To
 569 take into account the inclination of the probe, and
 570 find reliable plasma parameters, one should also
 571 multiply the total current by a geometric factor of
 572 $\pi r_p^2 / S_{\text{face}}$ from eq.(6) giving a dimensionless fac-
 573 tor of $1/(\cos \vartheta + [L_p/r_p] \times \sin \vartheta)$. This allows the
 574 recovering of the same amplitude for all bumped
 575 $I(V)$. The extracted values of n_e and T_e are plot-
 576 ted in fig.15-(b) and (c) using this correction, and
 577 plotted in fig.15-(d) and (e) without the correc-
 578 tion (n_e strongly decreases with the angle). From
 579 Fig. 15-(b) and (c) it is clear that the classical ϕ_p -
 580 determination method gives the more reliable val-
 581 ues of temperature and density (the deviation of T_e
 582 values between each inclination is negligible com-
 583 pared to other methods). We have then $T_e \approx 1.2$ eV
 584 and $n_e \approx 1.3 \times 10^{16} \text{ m}^{-3}$. Since the OML model
 585 remains valid in RF-plasmas³⁴, and that ions are
 586 unmagnetized, we extracted $n_i^{\text{OML}} = 1.74 \times 10^{17}$
 587 m^{-3} (which is within the typical errorbar for OML
 588 model) and $T_e^{\text{OML}} = 2.69$ eV, which are overesti-
 589 mated compared to the previous method.

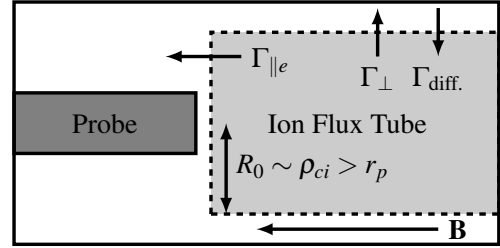


FIG. 16. Sketch of the fluid model. The flux tube is de-
 limited by the dashed line. The inclination ϑ is 0° .

590 By comparison, in the absence of magnetic field,
 591 the bump method to find the plasma potential makes
 592 no sense (since there is no bump) and both classi-
 593 cal and intersection methods are alike and give the
 594 same value of the plasma potential. Therefore the
 595 self-consistent algorithm gives an electron density
 596 of the order of $5.32 \times 10^{15} \text{ m}^{-3}$ and an electron tem-
 597 perature of 3.47 eV (for the same discharge param-
 598 eters as with $\|\mathbf{B}\| \neq 0$).

599 B. Fluid model approach

600 As suggested by Mihaila and Rozhansky^{16,23}, the
 601 bump on $I(V)$ characteristics could be induced by
 602 density depletion within the flux tube.

603 The cylindrical flux tube connected from the
 604 probe to the reactor's wall is filled by electrons us-
 605 ing a single channel, which is the lateral area of
 606 the cylinder. Due to magnetic confinement and for
 607 grazing incidences, the perpendicular current arises
 608 thanks to collisions with neutrals. During a $I(V)$
 609 measurement for $V > \phi_p$, one pumps the electrons
 610 inside the flux tube, which makes the local elec-
 611 tron density decreases. If the pumped electron cur-
 612 rent is larger than the refill perpendicular one, then
 613 the collected current at the probe decreases with
 614 phi (the bump origin). But when the probe poten-
 615 tial is increased further, the sheath extent around it
 616 also increases, which artificially makes the cylindri-
 617 cal flux tube diameter wider. Consequently, when
 618 $V \gg \phi_p$, the electron perpendicular current com-
 619 pensate the pumped one and the collected current
 620 increases again. Now for larger incidences, the per-
 621 pendicular current always overcomes the pumped
 622 one, which explains the experimentally observed
 623 disappearance of the bump for $\vartheta > 12^\circ$.

624 In the meantime, there is another mechanism in-
 625 volving mainly ions: it is the plasma pumping via
 626 perpendicular ion current due to the positive bias-
 627 ing of the flux tube with respect to the surround-
 628 ing plasma potential. This mechanism has already
 629 been invoked to explain the early electron satura-
 630 tion of the $I(V)$ characteristics in the case of planar

631 probe²³ in magnetized plasmas. The typical scale
632 length of these perpendicular ion currents is the ion
633 gyroradius. To explain the bump, this mechanism
634 can be divided in three regimes occurring when the
635 probe potential overcomes the plasma potential:

- 636 1. When the transverse (perpendicular to \mathbf{B})
637 ion current is lower than the electron saturation
638 current collected by the probe, the space charge
639 of the sheath is electropositive and consequently
640 the flux tube potential “follows” the probe potential.
641 The density depletion can first appear in that regime.
642
- 643 2. When the transverse ion current is exactly
644 equal to the electron saturation current collected
645 by the probe, the sheath between the probe and
646 the flux tube disappears and the collected current
647 can decrease because the flux tube density
648 decreases with the probe potential.
649
- 650 3. Finally when the transverse ion current is
651 higher than the electron saturation current
652 collected by the probe, electrons must be
653 accelerated in the sheath to balance the ion
654 current and thus the sheath drop is reversed. The
655 sheath space charge becomes electronegative
656 and the flux tube potential tends to saturate
657 compared to the probe potential. This regime
658 accounts for long and thin flux tube.

659 Nevertheless, plasma diffusion is more and more
660 efficient as the flux tube is widening. So in the third
661 regime, with the saturation of the flux tube potential,
662 the pumping also saturates and the density depletion
663 can be cancelled resulting in a classical increase
664 of the current in the last part of the $I(V)$ characteristics
665 (beyond the bump).

666 Finally there is an optimum point for which the
667 pumping is maximum compared to cross diffusion,
668 and this is at this working point the bump appears to
669 be the higher because of the strong negative slope
670 just following the maximum of the bump. Actually,
671 the bump does not mean there is an increase of
672 current compared to an $I(V)$ characteristics with no
673 bump, on the contrary it means a decrease of current.
674

675 The complexity of the phenomenon can only be
676 explained by a mass and current conservation taking
677 into account the growing of the flux tube radius
678 with the potential.

679 The model:

680 Rozhansky *et al.*²³ showed that the ion flux tube
681 has a characteristic radius of $R_0 \sim \rho_{ci}$, and a length
682 L (this ion flux tube connected to the probe also

683 contains the electron flux tube of radius $\rho_{ce} \ll \rho_{ci}$).
684 Due to their cyclotron motion, electrons are trapped
685 in both ion and electron tubes and can only leave
686 them through the ends, producing a parallel net current
687 of $J_{e,\text{sat.}} \times \pi R_0^2$. To ensure current and quasi-
688 neutrality conservation in the ion tube, there must
689 be a perpendicular ion flux through the cylindrical
690 surface so that, $J_{i,\text{sat.}} \times 2\pi R_0 L \approx J_{e,\text{sat.}} \times \pi R_0^2$. In
691 this regime, where the perpendicular current can
692 be higher than the electron saturation current on
693 the probe, the potential gap can reverse in front
694 of the probe (electronegative sheath) accelerating
695 electrons and repelling ions. Thus, one can neglect
696 the parallel ion flux on the probe side (in the
697 case of an electropositive sheath, the ion current on
698 the probe surface can also be neglected compared
699 to electron current, still assuming that the electron
700 current is close to its saturation value).

701 In the following we use current continuity for
702 ions in order to obtain a first order ODE that gives
703 the density of the flux tube with respect to the probe
704 potential. Using Laframboise’s theory, this tube
705 density (or “local plasma density”) gives the electron
706 fraction that will be collected by the probe regarding
707 its potential V . An analytic expression of the
708 collected current can be then provided.

709 As shown in the last sections, the pumping is
710 enhanced by perpendicular (to \mathbf{B}) RF and DC
711 currents^{21,22}. But periodic RF current can be reduced
712 to an averaged DC over one a period. That is why
713 the model is steady state, and only DC quantities
714 are considered. Finally, to prevent the tube
715 density to drop to zero, we assume the presence of
716 a source term S_0 , so that,

$$\iiint_{\text{tube}} S_0 \, d\tau = 2 \times \pi R_0^2 \times \frac{1}{2} n_0 \langle v_e \rangle, \quad (12)$$

717 where n_0 is the bulk plasma density (outside the ion
718 flux tube region) and n_t , the ion flux tube density
719 ($n_0 \geq n_t$). This term fills the tube at the same rate
720 electrons leave it from both ends (which is an over-
721 estimation of the “real” S_0 source term).

722 From the stationary ion continuity equation, we
723 have $\nabla \cdot \mathbf{\Gamma}_i \sim \nabla \cdot \mathbf{\Gamma}_{i,\perp} = S_0$. Perpendicular ion flux
724 is separated in two parts: lateral mobility $-\mu_i n_t \nabla \phi$
725 and the diffusion flux $-D_{\perp} \nabla n_t$. Integration of all
726 ion fluxes through the whole tube using Gauss’s law
727 gives:

$$\frac{n_0 \langle v_e \rangle}{2L} R_0 = - \left(D_{\perp} \frac{\partial n_t}{\partial r} \Big|_{R_0} + n_t \mu_i \times \frac{\partial \phi}{\partial r} \Big|_{R_0} \right) \quad (13)$$

728 In the presence of a strong radial electric field (and
729 especially in a cold plasma), the ion drift velocity
730 is larger than the thermal velocity, thus $\rho_{ci} =$
731 $v_{\perp} / \omega_{ci} = (v_{\text{drift}}^2 + v_{i,\text{Th.}}^2)^{1/2} / \omega_{ci} \sim |v_{\text{drift}}| / \omega_{ci} =$
732 $-\partial_r \phi / B \omega_{ci}$ (all at R_0). Recalling that $R_0 \sim \rho_{ci}$,

733 equation (13) rewrites as,

$$\frac{n_0 \langle v_e \rangle}{2LB\omega_{ci}} \times \frac{\partial \phi}{\partial r} \Big|_{R_0} = \left(D_{\perp} \frac{\partial n_t}{\partial r} \Big|_{R_0} + n_t \mu_i \times \frac{\partial \phi}{\partial r} \Big|_{R_0} \right) \quad (14)$$

734 Now using the chain rule, $\partial n_t / \partial r|_{R_0} = \partial n_t / \partial \phi \times$
 735 $\partial \phi / \partial r|_{R_0}$, one will get the following first order
 736 ODE at the radius $r = R_0$:

$$\frac{\partial n_t}{\partial \phi} = -\frac{\mu_i}{D_{\perp}} n_t + \frac{n_0 \langle v_e \rangle}{2\omega_{ci}BLD_{\perp}} \quad (15)$$

737 The perpendicular mobility can also be written as a
 738 conductivity depending on the current nature (col-
 739 lision, inertial, viscosity, anomalous,...). With the
 740 initial condition of $n_t(\phi = \phi_p) = n_e$ since there is
 741 no sheath nor spatial potential variation at plasma
 742 potential, one will get :

$$n_t(V) = n_{\infty} + (n_0 - n_{\infty}) \exp \left[\frac{\mu_i}{D_{\perp}} (V - \phi_p) \right], \quad (16)$$

743 where V is the probe potential and $n_{\infty} = n_0 \times$
 744 $\langle v_e \rangle / 2\mu_i B \omega_{ci} L$. Here we assumed that the flux tube
 745 potential equals the probe one. Although generally,
 746 $\phi_t = f(V) \geq V > \phi_p$.

747 Equation 16 exhibits an exponential decay of the
 748 density with V . This strong depletion of the flux
 749 tube as soon as the biased potential of the tube
 750 is higher than the surrounding plasma potential is
 751 needed to see the bump rising. For lower decay
 752 (for ex. $\sim 1/(V - \phi_p)$ or $\sim 1/(V - \phi_p)^2$) the bump
 753 does not appear because of the expansion of the
 754 sheath which increases the lateral surface of the flux
 755 tube and hence the total perpendicular current more
 756 rapidly that the density is depleted. This also
 757 explains why at higher probe potential value, when
 758 the exponential decay saturates, the current rises up
 759 again due to sheath expansion. Actually there is a
 760 competition between the diffusion D_{\perp} across the
 761 lateral surface of the tube versus the perpendicular
 762 current due to ion mobility μ_i as it can be seen in
 763 equation 16.

764 Next to fit the sheath expansion above V_p in a
 765 magnetic field parallel to the probe, one uses the
 766 Laframboise⁹ model which showed that the portion
 767 of plasma density actually touching a probe and
 768 thus collected, n_{eff} , is given by the relation,

$$n_{\text{eff}}(\xi) = \frac{2n_t(\xi)}{\sqrt{\pi}} \left[\sqrt{\xi} + \frac{\sqrt{\pi}}{2} e^{\xi} \text{erfc} \sqrt{\xi} \right] \quad (17)$$

769 for $\xi = e(V - \phi_p) / k_B T_e$. Finally, the collected cur-
 770 rent on the probe is simply given by

$$I_e(V) = \frac{1}{2} e n_{\text{eff}}(V) \times \langle v_e \rangle S_e \quad (18)$$

771 where S_e is given by eq.(9), and the number of elec-
 772 tron Larmor radii (N_{elr}) is given as fitting param-
 773 eter.

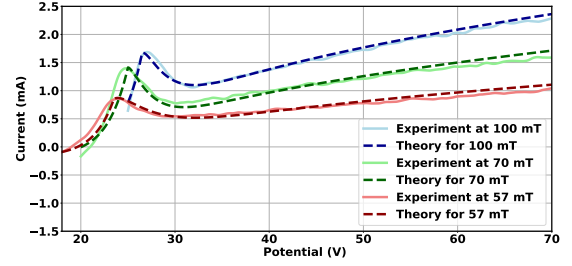


FIG. 17. Comparison of the 1D fluid model with the experiment. Probe had $\vartheta = 0^\circ$ inclination angle in 200 W-RF plasma at 1.2 Pa for several $\|\mathbf{B}\|$.

744 This model is compared with the experimental
 745 data in figure 17 for a magnetic field of 57, 70 and
 746 100 mT in a 200 W-RF and 1.2 Pa Helium plasma
 747 (the probe was parallel to \mathbf{B}). For $V < \phi_p$ the expo-
 748 nential $J_{e,\text{sat}} \times \exp(e(V - \phi_p) / k_B T_e) S_e$ part of the
 749 electronic current is considered.

750 The number of Larmor radii, N_{elr} , goes from 0.1
 751 to 5 with increasing $\|\mathbf{B}\|$ in Eq. (9). The limit den-
 752 sity in the flux tube, n_{∞} is close to $n_0 / 10$: that
 753 means that the measurement heavily depletes the
 754 magnetic flux tube. Moreover, the model suggests
 755 that the plasma potential is on the top of the bump
 756 as proposed by Dote and Mihaila : the pumping
 757 mechanism starts when $V > \phi_p$ according to the
 758 theory. Since electrons are way much mobile than
 759 ions along B , as soon as the probe potential is above
 760 the plasma potential, electrons of the flux tube are
 761 flushed towards the probe. Moreover, as pointed out
 762 by eq.(3), the flux tube itself has its own potential
 763 (slightly above the bulk plasma potential) since it is
 764 connected to the probe and thus somehow biased.

765 Finally, according to this theory, the prior param-
 766 eter is actually the probe surface facing the mag-
 767 netic field lines (i.e. the width of the magnetic flux
 768 tube). Therefore, a bump could appear on a plane
 769 probe characteristics or a spherical probe characteris-
 770 tics as well, if the facing surface is small enough
 771 corresponding more or less to a disk surface having
 772 a radius of the order of ρ_{ce} .

803 V. CONCLUSION

804 Langmuir probe measurements in the presence of
 805 a magnetic field are of a paramount importance in
 806 plasma physics. Understanding and exploiting $I(V)$
 807 characteristics from a cylindrical Langmuir probe
 808 in such conditions is difficult, especially due to the
 809 presence of a bump in the curves for grazing inci-
 810 dences of the cylindrical probe with respect to the
 811 magnetic field lines. In this paper, the evolution of
 812 the $I(V)$ characteristics with respect to several dis-
 813 charge parameters (magnetic field amplitude, probe
 814 inclination, and pressure) was studied, in order to

815 provide a better understanding of cylindrical Lang-
816 muir probe measurements in magnetized plasmas.

817 We showed that the presence of the magnetic
818 field changes the general shape of the $I(V)$ curves,
819 because of the breaking-up of the plasma isotropy:
820 the particles are not collected by the probe from all
821 possible directions anymore but from a flux tube,
822 connected to it from one end, and to the reactor's
823 wall to the other. That is why the general shape
824 of the characteristics tends to an asymmetric double
825 probe (or tanh-shaped) one. We also showed
826 that for grazing incidences of the probe with re-
827 spect to B , a bump arises between the exponential
828 part and the electron saturation current one. The
829 bump vanishes as the probe inclination is increased,
830 or if the magnetic field amplitude is reduced. It
831 is also dependent on collisional processes, because
832 its amplitude decreases, when the gas pressure in-
833 creases. Finally, increasing the RF-power at the an-
834 tenna heightens the bump amplitude, and can even
835 make one appearing on the characteristics.

836 We argued that a probe measurement pumps
837 electrons from their flux tube while ions are ex-
838 pelled in the perpendicular direction (the electron
839 current is mainly parallel to magnetic field lines).
840 This density depletion as soon as probe potential
841 V overcomes the plasma one ϕ_p (*i.e.* as the probe
842 starts to attract electrons) can explain the presence
843 of the bump. This hypothesis is strengthened by
844 the pressure effects on the probe measurements:
845 increasing the gas pressure (thus increasing colli-
846 sions and therefore, perpendicular diffusion fluxes),
847 makes the bump vanish. By using a fluid model,
848 we corroborated the pumping mechanism of den-
849 sity (due to a competition between mobility and
850 diffusion) and validated the assumption of density
851 depletion in the flux tube connected to the probe.
852 Nevertheless this assumption is not enough to make
853 appear the bump, the density decay in the flux tube
854 must be stronger than the perpendicular expansion
855 of the flux tube with V , that is why the exponential
856 decay from our model is needed.

857 We have finally compared different methods for
858 extracting both n_e and T_e from bumped charac-
859 teristics, which are not very usual in the con-
860 text of probe measurements. We showed that the
861 classical method of plasma potential determination
862 (where dI/dV is maximum) stays the most repro-
863 ducible method to access this important parameter,
864 although previous studies argued that the plasma
865 potential coincides with the bump one. A lot of
866 work is still needed to provide a complete theory
867 that exploits bumped characteristics, especially to
868 know the good collecting surfaces of the probe, and
869 the good mobility and diffusion parameters to put
870 in the model.

871 ACKNOWLEDGEMENTS

872 This work has been carried out within the frame-
873 work of the French Federation for Magnetic Fusion
874 Studies (FR-FCM) and of the Eurofusion consor-
875 tium, and has received funding from the Euratom
876 research and training programme 2014-2018 and
877 2019-2020 under grant agreement No 633053. The
878 views and opinions expressed herein do not neces-
879 sarily reflect those of the European Commission.

- 880 ¹M. A. Lieberman and A. J. Lichtenberg, *Principles Of Plasma*
- 881 *Discharges And Materials Processing*, edited by Wiley (Wiley
- 882 - Interscience, 2005).
- 883 ²F. Chen, *Introduction to Plasma Physics and Controlled Fu-*
- 884 *sion*, edited by N. Y. Academic Press Inc. (Springer US, 1984).
- 885 ³H. M. Mott-Smith and I. Langmuir, *Physical Review* **28**, 727
- 886 (1926).
- 887 ⁴J. Allen, R. Boyd, and P. Reynolds, *Plasma Sources Science*
- 888 *And Technology* **18**, 035012 (2009).
- 889 ⁵J. Allen, *Physica Scripta* **45**, 497 (1992).
- 890 ⁶I. B. Bernstein and I. N. Rabinowitz, *Physics Of Fluids* **2**, 119
- 891 (1959).
- 892 ⁷I. D. Sudit and R. C. Woods, *Journal of Applied Physics* **76**,
- 893 4488 (1994).
- 894 ⁸J. Laframboise, *UTIAS Report* **10**, 1 (1966).
- 895 ⁹J. G. Laframboise and L. W. Parker, *Physics Of Fluid* **16**, 629
- 896 (1973).
- 897 ¹⁰J. G. Laframboise and J. Rubinstein, *Physics Of Fluid* **19**, 1900
- 898 (1976).
- 899 ¹¹D. Bohm, E. Burhop, and H. Massey, "The use of probes for
- 900 plasma exploration in strong magnetic fields," (McGraw-Hill,
- 901 New York, 1949) Chap. 2.
- 902 ¹²F. Chen, C. Etievant, and D. Mosher, *Physics Of Fluids* **11**,
- 903 811 (1968).
- 904 ¹³T. K. Popov, M. Dimitrova, P. Ivanova, J. Kovacic, T. Gyer-
- 905 gyek, R. Dejarnac, J. Stocke, M. A. Pedrosa, D. Lopez-Bruna,
- 906 and C. Hidalgo, *Plasma Sources Science and Technology* **25**,
- 907 033001 (2016).
- 908 ¹⁴J. Moritz, E. Faudot, S. Devaux, and S. Heurax, *Physics Of*
- 909 *Plasmas* **25**, 013534 (2018).
- 910 ¹⁵T. Dote and H. Amemiya, *Journal Of The Physical Society Of*
- 911 *Japan* **19**, 1915 (1964).
- 912 ¹⁶I. Mihaila, M. Solomom, C. Costin, and G. Popa, *Contribution*
- 913 *Of Plasma Physics* **53**, 96 (2013).
- 914 ¹⁷M. Usoltceva, E. Faudot, S. Devaux, S. Heurax, J. Ledig,
- 915 G. V. Zadivitskiy, R. Ochoukov, K. Crombe, and J.-M. Noter-
- 916 daeme, *Physics of Plasmas* **25**, 063518 (2018).
- 917 ¹⁸M. Usoltceva, E. Faudot, J. Ledig, S. Devaux, S. Heurax,
- 918 G. V. Zadivitskiy, R. Ochoukov, J. Moritz, K. Crombe, and J.-
- 919 M. Noterdaeme, *Review of Scientific Instruments* **86**, 10J124
- 920 (2018).
- 921 ¹⁹T. Dote and H. Amemiya, *Journal Of The Physical Society Of*
- 922 *Japan* **22**, 270 (1967).
- 923 ²⁰T. Dote and H. Amemiya, *Japan Journal Applied Physics* **8**,
- 924 818 (1969).
- 925 ²¹E. Faudot, *Plasma Physics and Controlled Fusion* **22**, 083506
- 926 (2015).
- 927 ²²K. Gunther and A. Carlson, *Contribution On Plasma Physics*
- 928 **34**, 484 (1994).
- 929 ²³V. Rozhansky, A. Ushakov, and S. Voskoboinikov, *Nuclear*
- 930 *Fusion* **39**, 613 (1999).
- 931 ²⁴A. Nedospasov and D. Uzdensky, *Contributions To Plasma*
- 932 *Physics* **34**, 478 (1994).
- 933 ²⁵P. Verplancke, R. Chodura, J. Noterdaeme, and M. Weinlich,
- 934 *Contributions To Plasma Physics* **36**, 145 (1996).

- 935 ²⁶E. Faudot, S. Devaux, J. Moritz, S. Heuraux, P. M. Cabrera, 947
936 and F. Brochard, *Review of Scientific Instruments* **86**, 063502 948
937 (2015). 949
- 938 ²⁷S.Devaux, E.Faudot, J.Moritz, and S.Heuraux, *Nuclear Mate-* 950
939 *rials and Energy* **12**, 908 (2017). 951
- 940 ²⁸P. A. Chatterton, J. Rees, W. Wu, and K. Al-Assadi, *Vacuum* 952
941 **42**, 489 (1991). 953
- 942 ²⁹F. Gerhard, *Low Pressure Plasmas and Microstructuring Tech-* 954
943 *nology*, edited by Springer (Springer-Verlag Berlin Heidel- 955
944 berg,, 2009). 956
- 945 ³⁰L. Viehland, T. Skaist, C. Adhikari, and W. Siems, *Contribu-* 957
946 *tions To Plasma Physics* **20**, 1 (2017), scattering He ion/He
neutral obtained from <https://fr.lxcat.net> (visited November
11th 2018).
- ³¹E. Faudot, S. Heuraux, M. Kubic, J. Gunn, and L. Colas,
Physics Of Plasmas **20**, 043514 (2013).
- ³²P. Chabert and N. Braithwaite, *Physics Of Radio-Frequency
Plasmas*, edited by C. U. Press (Cambridge University Press,
2011).
- ³³Y. B. Zhu, P. Zhang, A. Valfells, L. K. Ang, and Y. Lau, *Phys-
ical Review Letters* **110**, 265007 (2013).
- ³⁴F. Chen, *Proceedings of the Physical Society. Section B* **70**,
297 (1957).